RSC Advances

PAPER

View Article Online
View Journal | View Issue

CrossMark click for updates

Cite this: *RSC Adv.*, 2017, **7**, 4062

Solvothermal synthesis of magnetic $CoFe_2O_4$/rGO nanocomposites for highly efficient dye removal in wastewater†

Wenzhu Yin,[a] Shuo Hao[ab] and Huaqiang Cao*[a]

Magnetic $CoFe_2O_4$/reduced graphene oxide (rGO) (abbreviated as CFG) nanocomposites were fabricated by a simple solvothermal process. The structure and composition of the as-synthesized CFG nanocomposites were investigated by transmission electron microscopy (TEM), vibrating sample magnetometry (VSM), N_2 adsorption–desorption isotherms, X-ray diffraction (XRD), X-ray photoelectron spectroscopy (XPS), and Raman spectroscopy. TEM images show that the uniform $CoFe_2O_4$ NPs (~11 nm) are well dispersed on the rGO nanosheets. In addition, CFG has a high surface area (239.76 m^2 g^{-1}), exhibits a strong magnetic strength (59.20 emu g^{-1}), and can be easily separated from other constituents under an external magnetic field. When using organic dyes, such as rhodamine B (Rh B), methylene blue (MB), Congo red (CR), methyl orange (MO), and methyl green (MG), as the adsorbates, CFG showed a good adsorption performance, especially, ~100% for MB within 5 min. The maximum adsorption capacities for Rh B, MB, CR, and MG were 121.8, 93.5, 104.5, and 88.3 mg g^{-1}, respectively. The effect of certain variables, such as temperature, pH of the initial solution, adsorbent dose, and adsorbate species, was studied in detail. All results suggested that CFG can be used as an environmentally friendly and highly efficient reusable adsorbent material with a high adsorption capacity and a fast removal rate that can be used to remove organic dyes from wastewater.

Received 17th November 2016
Accepted 11th December 2016

DOI: 10.1039/c6ra26948f

www.rsc.org/advances

Open Access Article. Published on 16 Januar 2017. Downloaded on 16.02.26 20:25:33.
This article is licensed under a Creative Commons Attribution 3.0 Unported Licence.

1. Introduction

Organic dyes are widely used in the textile industry because they provide bright colors and exhibit favourable characteristics, such as being easily water-soluble, cheaper to produce, and easier to apply on the fabric. However, when these organic dyes are present in effluents, they are of serious concern because of their adverse effects to human health and environment.[1] Therefore, removing these dyes from the industrial effluents has been a major environmental concern in recent years.[2] Various methods, such as biological treatment, adsorption, chemical oxidation, photocatalytic degradation, and coagulation, have been used to remove dyes from dye-containing wastewater.[3–12] Among these methods, adsorption is a preferred route because of its low-cost, simplicity, and relatively low sludge production.[13–15] Therefore, it is very important to develop novel adsorbents with high adsorption capacity and fast separation rates for treating large volumes of wastewater.[16–19] Among the processes being proposed and/or developed, graphene-based adsorption is one of the most promising methods owing to the layered structure and high thermal and chemical stability of graphene and because of being highly efficient and less time-consuming.[20–23] However, the drawback regarding these methods is the separation of graphene, which limits its further applications.

In recent years, the application of magnetic particle technology to solve environmental problems has received considerable attention.[24–26] Magnetic separation has been recognized as a fast and effective technique for separating magnetic particles from multicompositions. Cobalt ferrite ($CoFe_2O_4$) nanocrystals with spinel structure have attracted significant attention for environmental remediation because of their outstanding properties, such as high saturation magnetization, and size- and shape-dependent magnetic behaviour.[27] Although some studies have reported the preparation and adsorption properties of $CoFe_2O_4$/graphene nanocomposites, the trivial process of preparation,[28] slow removal rate,[29] and low adsorption capacities[30,31] hinder their applications in industrial wastewater treatment, which still remains a challenging task. In addition, Chen[32] *et al.* reported a one-step method to prepare $CoFe_2O_4$–rGO by ball-milling, and the as-prepared $CoFe_2O_4$–

[a]*Department of Chemistry, Tsinghua University, Beijing 100084, P. R. China. E-mail: hqcao@mail.tsinghua.edu.cn*

[b]*College of Chemistry and Molecular Engineering, Zhengzhou University, Zhengzhou 450001, P. R. China*

† Electronic supplementary information (ESI) available: C/C_0 *versus* time plots for Rh B solutions at different pH values condition was presented in Fig. S1, pseudo-first-order kinetics for adsorption of Rh B solution (220 mL, 10 μM) at pH = 7 condition was presented in Fig. S2, time-dependent removal of Rh B (220 mL, 10 μM) by CFG, GO and CFO at pH = 7 condition was presented in Fig. S3, time-dependent removal of Rh B by CFG. Inset: the images of absorb Rh B in 0 min (left) and 30 min (right) was presented in Fig. S4. See DOI: 10.1039/c6ra26948f

This journal is © The Royal Society of Chemistry 2017

Open Access Article. Published on 16 Januar 2017. Downloaded on 16.02.26 20:25:33.
This article is licensed under a Creative Commons Attribution 3.0 Unported Licence.

rGO could be used for organic dye removal by photocatalytic degradation. Although photocatalytic degradation has many advantages, without light, the process of dye degradation can not occur. Furthermore, the photocatalytic degradation is a complex radical reaction, and the by-products may result in secondary pollution. Therefore, designing and tailoring $CoFe_2O_4$ hierarchical composite structures could be an appealing choice to address these challenges.

In the present study, cobalt ferrite ($CoFe_2O_4$) was immobilized on rGO *via* a solvothermal route. The as-prepared $CoFe_2O_4$/reduced graphene oxide (rGO) (abbreviated as CFG) nanocomposites have a large specific surface area, monodispersity of $CoFe_2O_4$ NPs, and are easy to separate under an external magnetic field. This means that CFG is a recyclable adsorbent for dye removal. Note that the adsorption capacities of CFG for dyes (initial dye concentration of 10 μM) are much higher than that of other magnetic adsorbents,[33–38] demonstrating that the magnetic CFG nanocomposite is a promising material in the fields of separation/purification-related technologies.

2. Experimental

2.1. Chemicals and reagents

All reagents used in this experiment were of analytical grade and used as received without further purification. Natural graphite flakes with an average particle size of 50 mesh were obtained from Qingdao Tianshengda Graphite Co., Ltd. Potassium permanganate ($KMnO_4$), sodium nitrate ($NaNO_3$), ferric chloride hexahydrate ($FeCl_3 \cdot 6H_2O$), cobalt chloride hexahydrate ($CoCl_2 \cdot 6H_2O$), rhodamine B (Rh B), methyl green (MG), methylene blue (MB), Congo red (CR), and methyl orange (MO) were purchased from Sinopharm chemical reagent Co., Ltd. Sulfuric acid (H_2SO_4, 99%), hydrochloric acid (HCl), hydrogen peroxide (H_2O_2, 30%), hydrazine hydrate ($N_2H_4 \cdot H_2O$, 80%), ethylene glycol, and ethanol were supplied by Beijing chemical reagent Co., Ltd. Deionized water (DIW) was obtained using a Milli-Q water purification system (Millipore, Billerica, MA, USA).

2.2. Synthesis of the CFG nanocomposites and $CoFe_2O_4$ NPs (CFO)

Graphene oxide (GO) was synthesized from natural graphite powder by the modified Hummers method as described hereinafter.[39] CFG nanocomposites were synthesized *via* a solvothermal process described as follows. Typically, 40 mg of GO was dispersed in a 20 mL of ethylene glycol and DIW cosolvent (v/v = 3 : 1) with sonication for 2 h. At the same time, 135 mg of $FeCl_3 \cdot 6H_2O$ (0.5 mmol) and 59.5 mg of $CoCl_2 \cdot 6H_2O$ (0.25 mmol) were dissolved in 15 mL of DIW. After the GO dispersion was added, the resulting solution was stirred at room temperature for 5 h for the ion exchange. Then, $N_2H_4 \cdot H_2O$ (3 mL), which acted as both reducing agent and mineralizer, was added into the GO solution and the mixture was stirred for 0.5 h. The mixture was then transferred to a 50 mL Teflon-lined stainless steel autoclave and heated at 180 °C for 12 h. The product was collected, washed with DIW and absolute ethanol several times, and finally dried at 60 °C for 5 h. Bare $CoFe_2O_4$ was also synthesized *via* a similar route without adding GO.

2.3. Characterizations

XRD spectra (Bruker D8 advance) with Cu Kα radiation (λ = 1.5406 Å, 40 kV, 40 mA) were obtained in the 2 theta range from 5 to 80° for the crystal analysis of the sample. X-ray photoelectron spectroscopy (XPS) was carried out using a 250XI X-ray photoelectron spectrometer with an Al Kα radiation (1486.7 eV) as the excitation source at a base pressure of 1×10^{-8} Torr. All binding energy values were referenced to the C 1s peak of contaminant carbon at 284.8 eV. Raman spectra were obtained using an inVia-Reflex spectrometer at an excitation wavelength of 633 nm. The microstructure of CFG was analyzed by transmission electron microscopy (TEM, Hitachi H7650B, operating at 80 kV), high-resolution transmission electron microscopy (HRTEM, JEOL JEM-2100F, operating at 200 kV), and scanning electron microscopy (SEM, Hitachi S-3400 N II) coupled with energy-dispersive X-ray spectroscopy (EDX).

The specific surface area and the pore-size distribution were determined by N_2 adsorption/desorption isotherms at 77 K using a Thermo Fisher Scientific Surfer Gas Adsorption Porosimeter. Before measurements, samples were degassed at 300 °C for 6 h. The specific surface area was calculated using the Brunauer–Emmett–Teller (BET) method based on the adsorption data within the linear relative pressure (P/P_0) range of 0.04–0.35. The pore-size distribution was calculated from the corresponding adsorption branch of the N_2 isotherm by the Horvath–Kawazoe (HK) method for micropores and the Barrett–Joyner–Halenda (BJH) method for mesopores.

The magnetic properties were determined by vibrating sample magnetometer (VSM, Lakeshore, Model 7300 series). Absorption spectra were obtained using a Perkin Elmer Lambda 35 UV-Vis spectrophotometer.

2.4. Adsorption studies

Adsorption tests were typically carried out by stirring 50 mg of CFG in 200 mL of water solution containing 1×10^{-5} M organic dye in a 500 mL glass bottle. Experiments were also performed to determine the effects of varying both the adsorbent concentration and pH of the solution. All the experiments were carried out at a constant speed of 200 rpm under magnetic stirring. During each run, aliquots of 0.1 mL were withdrawn from the mixture at regular intervals of time, diluted, and centrifuged for 10 min at 2000 rpm. Subsequently, the absorbance of the supernatant solution was measured. The dye concentration was spectrophotometrically determined using a UV-Vis spectrophotometer and a 1 cm path-length cell to monitor the absorbance at λ_{max}, corresponding to the maximum absorbance of the analyzed dyes. On the basis of the Lambert–Beer's law, the absorbance range was set from 0.1 to 1.0. Calibration curves were plotted to establish the relationship between absorbance and concentration of the standard dye solutions. The pH measurements were performed using a PHS-3E pH meter.

Open Access Article. Published on 16 Januar 2017. Downloaded on 16.02.26 20:25:33.
This article is licensed under a Creative Commons Attribution 3.0 Unported Licence.

2.5. Calculations

The removal (%) of the dyes was defined according to the following equation:

$$\text{Removal (\%)} = (1 - C_1/C_0) \times 100\% \quad (1)$$

where C_0 (mg L^{-1}) is the initial dye concentration before removal and C_1 (mg L^{-1}) is the concentration of the dye remained in the solution after treatment for 30 min.

The amount of dye adsorbed by the CFG composite at each time interval t, q_t, was calculated by the following mass balance equation:

$$q_t = (C_0 - C_t)V/m \quad (2)$$

where q_t is the amount of dye adsorbed per unit weight of CFG at any time t (mg g^{-1}); C_0 and C_t are the initial and liquid phase concentrations of the dye solution at any time t (mg L^{-1}), respectively; V is the volume of the dye solution (200 mL); and m is the mass of CFG used (50 mg). For the experiments with different initial dye concentrations, the amount of CFG was 50 mg.

3. Results and discussion

3.1. Synthesis mechanism and characterization of the CFG nanocomposites

The as-prepared CFG nanocomposites have been synthesized with $CoFe_2O_4$ NPs (~11 nm) anchored on a rGO framework *via* a solvothermal method (Scheme 1). Fe^{3+} and Co^{2+} were supported on the graphene surface *via* ion exchange. Then, $N_2H_4 \cdot H_2O$ not only provides OH^- for the formation of $Fe(OH)_3$ and $Co(OH)_2$, but also acts as a reducing regent for reducing GO into rGO. In addition, hydrazine hydrate coordinates with Fe^{3+} and Co^{2+} and plays a role of capping reagent to control the growth of $CoFe_2O_4$ NPs. Finally, the $CoFe_2O_4$ NPs supported on rGO were obtained.

The morphology, structure, and composition of the as-prepared CFG nanocomposites were investigated by TEM and EDX. As shown in Fig. 1a, it can be clearly seen that GO displayed a wrinkled paper-like structure of the ultrathin sheets and stacking of the sheets. Furthermore, $CoFe_2O_4$ NPs can deposit on the surface of the rGO nanosheet in a dense and orderly manner (Fig. 1b and c) and their size on the CFG nanocomposites are in the range of 6–17 nm, with an average particle size of about 11 nm (Fig. 1d). In addition, we further examined the crystal structure of $CoFe_2O_4$ NPs on graphene by HRTEM (Fig. 1e), and the *d*-spacing was about 0.29 nm, which was attributed to the lattice spacing of the (220) planes of $CoFe_2O_4$. When compared with the as-prepared CFG, the size and shape of the $CoFe_2O_4$ NPs barely changed and were still firmly attached on the rGO nanosheet after the 6th regeneration cycle (Fig. 1f), indicating that an excellent adhesion between rGO and the $CoFe_2O_4$ NPs was achieved. The stability of the CFG structure provides the possibility of recycling. Moreover, the EDX spectrum (Fig. 1g) confirmed the presence of C, Co, Fe, and O in the CFG nanocomposites. Also, the atomic% (Table 1) can further confirm the structure of the CFG nanocomposites. Moreover, the content of $CoFe_2O_4$ in the CFG nanocomposites is about 74.6%. Additionally, Fig. 1h shows the TEM images of bare $CoFe_2O_4$ (CFO), which was synthesized *via* a similar route without adding GO. In the absence of GO, the as-prepared CFO easily formed aggregates.

The XRD patterns of the obtained CFO and CFG nanocomposites are shown in Fig. 2. The peaks at 30.2°, 35.6°, 43.2°, 53.7°, 57.1°, 62.6°, and 74.5° are indexed to the characteristic

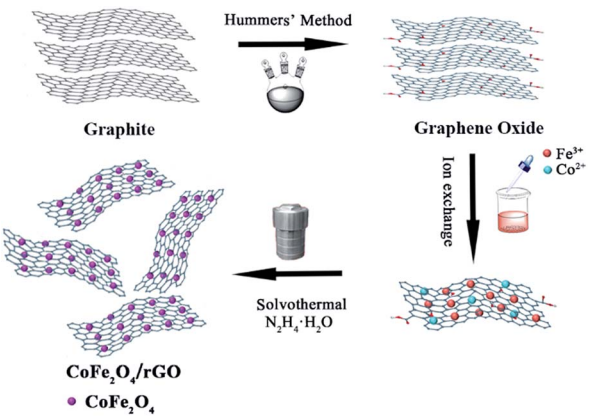

Scheme 1 Schematic of the *in situ* synthetic route for the CFG nanocomposites.

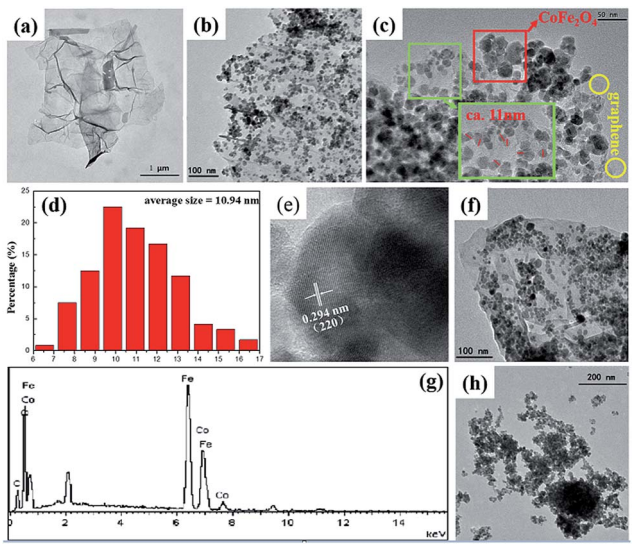

Fig. 1 TEM images of (a) GO, (b) CFG before removal, (f) CFG after the 6th regeneration cycle, and (h) CFO; (c and e) TEM and HRTEM images of CFG; (d) size distribution of the $CoFe_2O_4$ NPs in the CFG nanocomposites; (g) EDX of the CFG nanocomposites.

Table 1 Weight (%) and atomic (%) of the CFG nanocomposites as obtained from the EDX spectra

Element	C	Co	Fe	O
Weight (%)	12.19	23.51	41.88	22.43
Atomic (%)	28.46	11.19	21.03	39.32

This journal is © The Royal Society of Chemistry 2017

Open Access Article. Published on 16 Januar 2017. Downloaded on 16.02.26 20:25:33.
This article is licensed under a Creative Commons Attribution 3.0 Unported Licence.

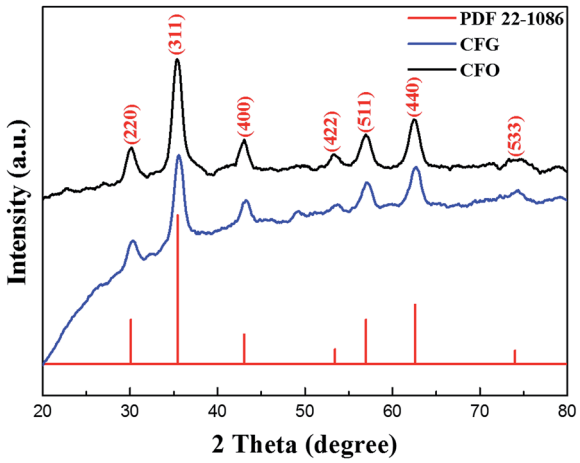

Fig. 2 XRD patterns of the CFO and CFG nanocomposites.

peaks of (220), (311), (440), (422), (511), (440), and (533) planes, respectively. All marked peaks were clearly indexed to the standard cobalt ferrite ($CoFe_2O_4$) (PDF 22-1086),[40] which is consistent with the EDX spectrum result. Note that no obvious diffraction peaks for rGO can be observed in the CFG nanocomposites, which might be due to the fact that the $CoFe_2O_4$ NPs are dispersed on the rGO surface, thus restraining the stacking of graphene layers in the composite.[41] According to the Scherrer equation, the average particle size of the $CoFe_2O_4$ NPs is about 14.58 nm, which is in good agreement with the value obtained from the TEM image.

Fig. 3a shows the Raman spectra of CFG, GO, and CFO. Curve (i) presents the as-synthesized $CoFe_2O_4$ sample at room temperature. Three major Raman active modes with broadening peaks at about 310, 470, and 670 cm^{-1} can be clearly observed, which are compared with the spectra of some previous reports, showing the specific characteristics (A_{1g}, E_g, $3T_{2g}$) of $CoFe_2O_4$ ferrite.[29] CFG (curve (ii)) and CFO share similar peaks in the frequency range from 250 to 750 cm^{-1} (about 307, 474, and 654 cm^{-1}), showing the existence of $CoFe_2O_4$ NPs in CFG. When compared with CFO, the CFG nanocomposite spectrum exhibits two Raman peaks at 1325 (D band) and 1595 cm^{-1} (G band), corresponding to graphene. The existence of these two bands in the CFG nanocomposites indicated that the graphene has been incorporated into the nanocomposite. In addition, when compared with GO, the D and G peaks of CFG shifted from 1325 to 1341 cm^{-1}, and from 1595 to 1596 cm^{-1}, indicating that GO has been reduced into rGO.[42,43] The peak intensity ratio of the D band (the symmetry A_{1g} mode) and the G band (the E_{2g} mode of sp^2 carbon atoms) could sensitively reflect the structural disorder degree of graphene. As a classical architecture with stacked π-conjugation, the precursor GO has an extremely small I_D/I_G ratio of 1.082. After reducing it with $N_2H_4 \cdot H_2O$, the product CFG had an even higher I_D/I_G ratio of 1.584, which could be explained by the structural disorder within the material or the intensively reduced size of the in-plane sp^2 conjugate domains.[44]

The N_2 adsorption/desorption isotherm exhibits an atypical IV-type curve with two steep uptakes ($P/P_0 < 0.01$, $P/P_0 > 0.97$)

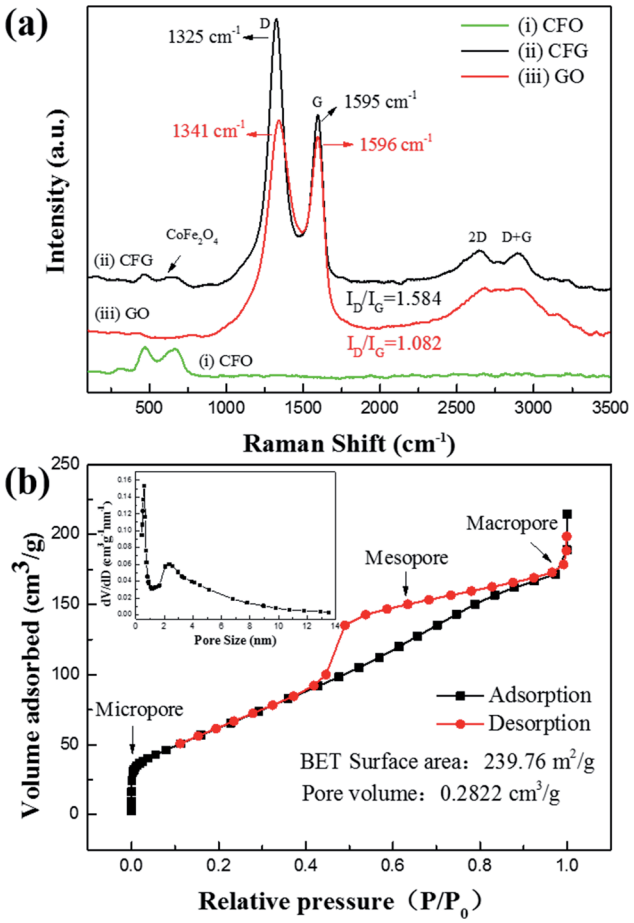

Fig. 3 (a) Raman spectra of CFG, CFO, and GO; and (b) nitrogen adsorption–desorption isotherm curves of CFG. Inset of (b) is the pore-size distribution curve for CFG.

and a hysteresis loop ($0.40 < P/P_0 < 0.95$), indicating the coexistence of micropores (<2 nm), mesopores (2–50 nm), and macropores (>50 nm) (Fig. 3b).[45] From the adsorption branch of the isotherm, the specific surface area was 239.76 $m^2\ g^{-1}$ and the total pore volume was 0.282 $cm^3\ g^{-1}$, calculated by the multipoint Brunauer–Emmett–Teller method. The pore-size distribution is concentrated in the range of a typical mesoporous structure (inset of Fig. 3b) and the most probable pore size is 4.76 nm, which was calculated by the Barrett–Joyner–Halenda model. The large specific surface area of CFG should guarantee its adsorption performance for dyes in water.

XPS measurement was used to study the surface components and the elements valences of the CFG. In this study, CFG nanocomposites were characterized by XPS, and charging of the samples was controlled using a charge neutralizer filament, which were calibrated using the adventitious C 1s peak with a fixed value of 284.8 eV. Fig. 4a shows the characteristic photoelectron peaks of the as-synthesized CFG with scan binding energy (BE) from 200 to 1000 eV, and no additional elements were detected except for the core or outer orbital level photoelectrons and Auger electrons of Fe, Co, C, and O. The high resolution spectrum of the C 1s regions for the identification of surface functionalities are fitted by seven component

Open Access Article. Published on 16 Januar 2017. Downloaded on 16.02.26 20:25:33.
This article is licensed under a Creative Commons Attribution 3.0 Unported Licence.

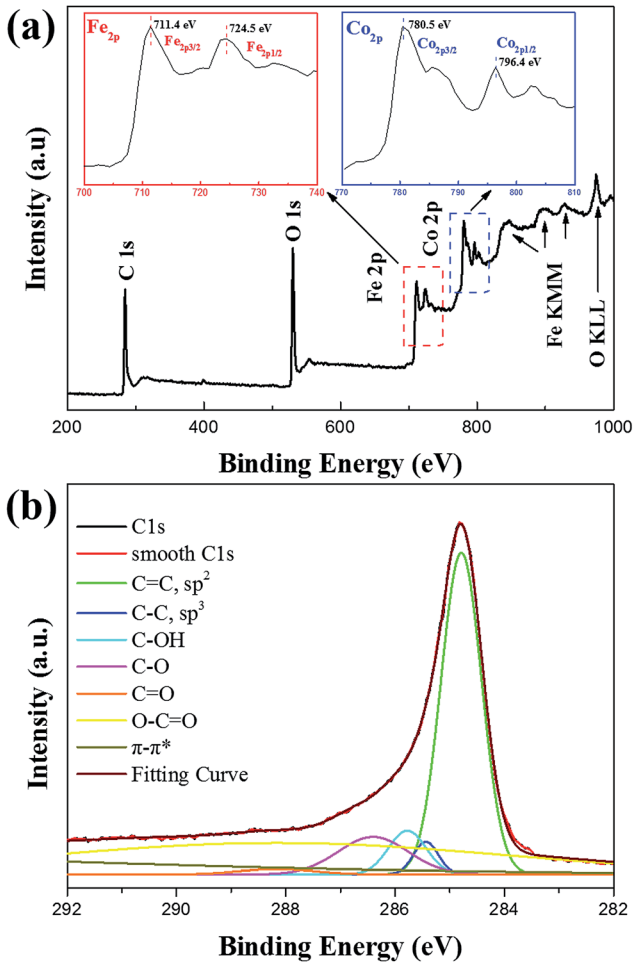

Fig. 4 XPS spectra: (a) wide-scan survey of the CFG nanocomposites and (b) C 1s spectrum of the CFG nanocomposites.

peaks as shown in Fig. 4b, which are assigned to sp^2 carbons (C=C, 284.8 eV), sp^3 carbons (285.5 eV), hydroxyl groups (C–OH, 286.0 eV), epoxy and ether groups (C–O, 286.6 eV), carbonyl groups (C=O, 287.6 eV), carboxyl groups (O–C=O, 288.7 eV), and π–π* shake-up transitions (289.9 eV). The relative contributions of the components associated with oxygenated and sp^3 carbon species in the CFG was significantly lowered, and the overwhelming percentage of graphitic carbon suggested the graphitized nature of the CFG nanocomposites.[46] From the Co 2p spectrum, it was found that the first two peaks, with binding energies of about 780.5 and 786.4 eV, correspond to Co $2p_{3/2}$ and its shake-up satellites, respectively, whereas the higher binding energy peaks around 795.5 and 802.6 eV were attributed to Co $2p_{1/2}$ and its shake-up satellites, respectively. The intense Co $2p_{3/2}$ shake-up satellite evidenced the presence of a large number of Co^{2+} species in the sample because the low-spin Co^{3+} cation only gave rise to much weaker satellite features than high-spin Co^{2+} with unpaired valence 3d electron orbitals.[47] In addition, two peaks of an Fe 2p level with binding energies of 711.4 and 724.5 eV were assigned to Fe $2p_{3/2}$ and Fe $2p_{1/2}$, respectively. This result clearly demonstrated the presence of Fe^{3+}. All the abovementioned analyses further confirmed the presence of $CoFe_2O_4$ nanocrystals on the surface of graphene nanosheets without any impurities.

Fig. 5 shows the magnetization curves of the as-prepared CFO and CFG nanocomposites measured at room temperature by VSM. The saturation magnetization (M_s) is 75.86 emu g^{-1} and 59.20 emu g^{-1} for the CFO and CFG nanocomposites, respectively. The decrease in the M_s can be attributed to the presence of nonmagnetic graphene. The magnetic property of the as-prepared CFG nanocomposite indicates that as an adsorbent, it can be easily separated from the solution phase within several minutes by inducing an external magnetic field.

3.2. Adsorption properties

3.2.1. Effect of solution pH. The pH of the initial dye solution may affect the active binding sites on the adsorbent surface and affect the chemistry of the aqueous system. Fig. 6a shows that CFG has the highest adsorbent efficiency for MB at pH = 7. The dye removal percentage is 98.6% at pH = 7, and upon increasing or decreasing pH, the adsorption capacity slightly decreased. It is well known that adsorption of an ionic dye is affected by the electrical properties of the adsorbent and solvent. Under highly acidic or alkaline conditions, protonation/deprotonation on the surface of CFG forms charges,[48] and the electrostatic interaction between CFG, ionic dyes, and H^+ or OH^- hinder the approach of ionic dyes to CFG, leading to a decrease in the adsorption efficiency. In addition, the CFG shows similar pH effects between MB and other dyes (Fig. S1†).

3.2.2. Dependence of removal efficiency on CFG dosage. The dependence of removal efficiency on dosage of the CFG adsorbent was investigated (Fig. 6b). The experiment was conducted by adding different adsorbent doses (25, 35, and 50 mg) in 200 mL of dye solution at pH = 7. The results showed that an increase in the mass of sorbent reduced the concentration of MB in the liquid phase. With an increase in the mass of sorbent, the dye removal percentage linearly increased up to a certain value, and then reached a plateau. By increasing the weight of

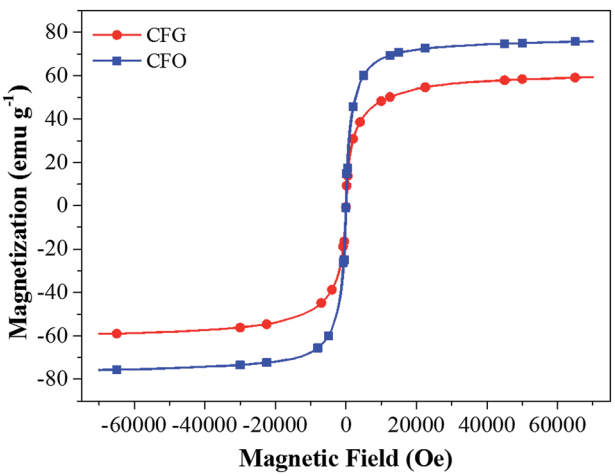

Fig. 5 Magnetization curves of the CFO and CFG nanocomposites at room temperature.

This journal is © The Royal Society of Chemistry 2017

Open Access Article. Published on 16 Januar 2017. Downloaded on 16.02.26 20:25:33.
This article is licensed under a Creative Commons Attribution 3.0 Unported Licence.

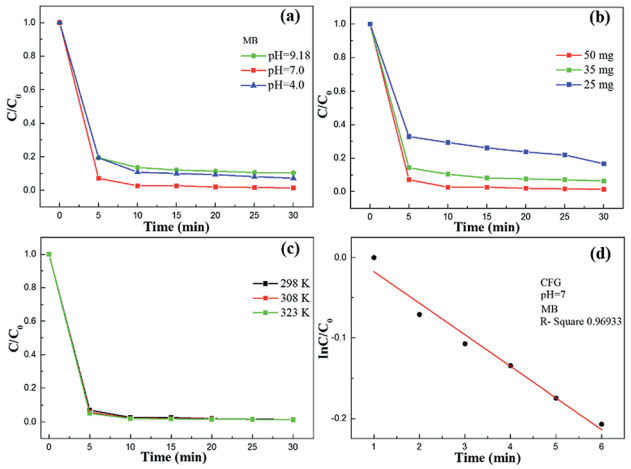

Fig. 6 C/C_0 *versus* time plots for (a) various solution pHs (b) various adsorbent dosages and (c) various solution temperatures; (d) pseudo-first-order kinetics for the adsorption of MB in solution (10 μM, 200 mL solution).

the adsorbent, the percent of dye removal could be enhanced, which was ascribed to the increase in the available active sites on the CFG surface.

3.2.3. The adsorption mechanism of CFG nanocomposites. The adsorption kinetics reflects the dye uptake rate and represents the adsorption efficiency of the adsorbent, therefore it determines the potential applications of CFG. Fig. 6c shows the kinetic analysis of the effect of temperature on the methylene blue adsorption. The adsorption slightly increases upon increasing the temperature, which is attributed to an increase in the mobility of dye molecules, and hence increases the interactions between the dye molecules and the active sites on the GO surface. This trend indicates that the adsorption process is endothermic. Additionally, when the temperature was increased, the viscosity of the solution decreased and the diffusion rate of the dye molecules increased.

As shown in Fig. 6d, the adsorption process is distinctly consistent with a pseudo first-order kinetics. The linear form of the pseudo first-order rate equation is given as follows:

$$\ln(q_e - q) = \ln q_e - k_1 t \quad (3)$$

where q_e and q are the amounts of methylene blue adsorbed on CFG (mg g^{-1}) at equilibrium and at various times t, respectively, and k_1 is the rate constant for the pseudo first-order adsorption model (min^{-1}).[49] A good linear relationship was observed, with a correlation coefficient (R^2) of 0.993, and the kinetic adsorption rate constant (k_1) was -0.039 min^{-1}. It is similar for the adsorption of MB by CFG, and CFG also shows a pseudo first-order adsorption kinetics for Rh B, as shown in Fig. S2.†

3.2.4. Adsorption and removal efficiency of CFG for dyes. The magnetic properties of the CFG adsorbents allowed their separation from water by applying a magnetic field, indicating that magnetic CFG provides a promising application for environmental remediation. In this study, the adsorption behavior of CFG was evaluated using MB as a model adsorbate. Four other organic dyes, including Rh B, MG, MO, and CR, were used to evaluate the adsorbent applicability. As compared with bared CFO and GO, CFG shows the best adsorption performance for MB, which clearly evidences that CFG possesses a significantly higher adsorption capacity for an organic dye (MB) than those of pure CFO and GO (Fig. 7a). Similar result was obtained for Rh B, MG, and CR (Fig. S3†). As it is known, the adsorption behavior of dye molecules may result from physical adsorption on the GO surface. Hydrophobic interactions (π–π stacking) could occur between the hydrophobic basal planes of the CFG nanocomposites and the aromatic rings of the dyes, leading to strong π–π stacking interactions under neutral conditions. The interactions between the dye molecules and adsorbent are mainly responsible for the superior adsorption of the CFG nanocomposites.

To investigate the adsorption capacity of CFG for MB, we immersed CFG (50 mg) in an aqueous solution of MB (1.0×10^{-5} M, 200 mL) for 30 min. Note that the adsorption rate of these dyes is independent of the changes in the temperature. A contact time of less than 5 min was invariably sufficient to reach an equilibrium. As shown in Fig. 7b, the adsorption band of the typical MB gradually disappeared with the increasing time, and the color of the solution disappeared after 10 min (inset of Fig. 7b). Similarly, CFG could completely adsorb Rh B within 30 minutes (Fig. S4†).

To investigate the potential application of CFG as an adsorbent for wastewater treatment, we carried out an adsorption experiment for the adsorption of MG, MR, and Rh B by CFG (Fig. 7c). The results of the experiment showed that CFG can also remove MG, MR, and Rh B quickly, and the maximum adsorption amounts of Rh B, MB, CR and MG were 121.8, 93.5, 104.5, and 88.3 mg g^{-1}, respectively. Fig. 7d shows that the removal efficiency of CFG for Rh B, MB, MG, MO, and CR at concentrations of 1.0×10^{-5} M reach to 98.0%, 98.6%, 84.0%, 54.9% and 86.4%, respectively. These results suggest that the as-prepared CFG nanocomposites show excellent removal performance for these dyes.

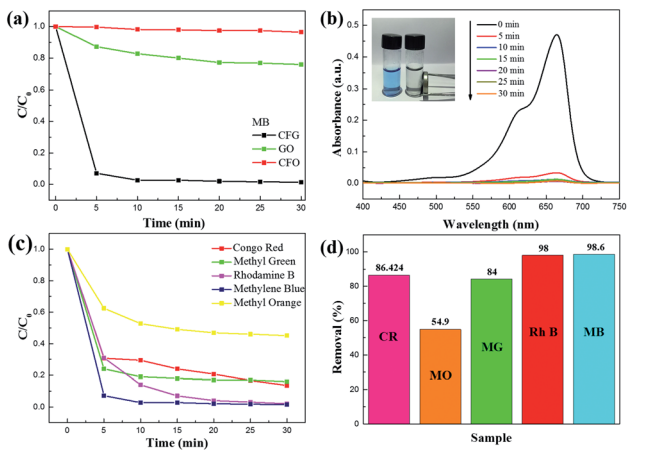

Fig. 7 (a) Time-dependent removal of MB by CFG, GO, and CFO; (b) time-dependent removal of MB by CFG; (c) time-dependent removal of different dyes by CFG, and (d) removal efficiency of different dyes by CFG.

Open Access Article. Published on 16 Januar 2017. Downloaded on 16.02.26 20:25:33.
This article is licensed under a Creative Commons Attribution 3.0 Unported Licence.

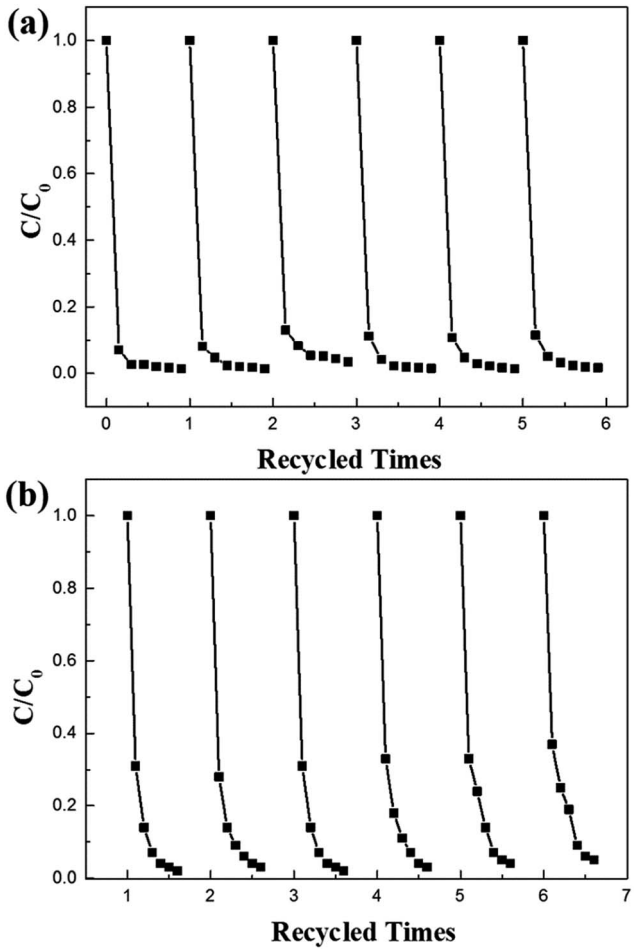

Fig. 8 C/C_0 *versus* time plots for the adsorption of (a) MB and (b) Rh B solution (200 mL) by recycled CFG (50 mg).

3.2.5. Recyclability of CFG for dye adsorption. Reusability is an important parameter for an adsorbent in practical applications. This is because the adsorbent cost is high and it can become a secondary pollutant to the environment if not reused. Therefore, it is necessary to evaluate the reusability of CFG. In this study, the used CFG adsorbent can be regenerated by magnetic separation, and then washed with ethanol for 30 min under magnetic stirring. As shown in Fig. 8, the removal efficiency for MB and Rh B at the first cycle of recyclability is close to 98.6% and 98.0%, respectively. Even after 6 cycles of regeneration, the removal efficiencies for MB and Rh B still reach to 98.5% and 98.0%, respectively. These results indicate that there is no noticeable loss in the adsorption capacity of CFG after regeneration. This suggests that CFG can exhibit high stability and recyclability after multiple cycles. Additionally, the CFG adsorbent can be easily recycled from water by a magnet, which is very important for industrial applications to avoid secondary pollution during wastewater treatment.

4. Conclusions

In summary, the magnetic CFG nanostructures were synthesized *via* a simple solvothermal process, and the monodispersed $CoFe_2O_4$ NPs had a uniform size of about 11 nm. CFG displayed a higher adsorption capacity for MB, MG, Rh B, and CR in water. The results demonstrated that CFG had a high adsorption capacity and high adsorption rate, and could be easily separated under an external magnetic field. The maximum adsorption capacities of CFG for Rh B, MB, CR, and MG were 121.8, 93.5, 104.5, and 88.3 mg g^{-1}, respectively. Furthermore, benefiting from its high saturation magnetization (over 59.20 emu g^{-1}), the as-obtained CFG adsorbent could be easily separated from the solution by a magnet. The magnetic CFG adsorbent could be regenerated and reused for organic dye removal, thus the magnetically separable CFG is a promising material in the fields of separation/purification-related technologies without introducing foreign pollutants.

Acknowledgements

This work was jointly supported by the National Program on Key Basic Research Project (973 Program, No. 2013CB933804) and the National Natural Science Foundation of China (No. 21271112, 21231005).

Notes and references

1 M. Rafatullah, O. Sulaiman, R. Hashim and A. Ahmad, *J. Hazard. Mater.*, 2010, **177**, 70–80.
2 B. D. C. Ventura-camargo and M. A. Marin-morales, *Textiles and Light Industrial Science and Technology*, 2013, **2**, 85–103.
3 F. C. Wu and R. L. Tseng, *J. Hazard. Mater.*, 2008, **152**, 1256–1267.
4 X. F. Wu, W. Wang, F. Li, S. Khaimanov, N. Tsdaeva and M. Lahoubi, *Appl. Surf. Sci.*, 2016, **389**, 1003–1011.
5 S. J. You, B. Liu, Y. F. Gao, Y. Wang, C. Y. Tang, Y. B. Huang and N. Q. Ren, *Electrochim. Acta*, 2016, **214**, 326–335.
6 X. Han, S. Y. Dong, C. F. Yu, Y. Y. Wang, K. Wang and J. H. Sun, *J. Alloys Compd.*, 2016, **685**, 997–1007.
7 S. Shukla and M. A. Oturan, *Environ. Chem. Lett.*, 2015, **13**, 157–172.
8 H. Zangeneh, A. A. L. Zinatizadeh, M. Habibi, M. Akia and M. H. Isa, *J. Ind. Eng. Chem.*, 2015, **26**, 1–36.
9 A. Ahmad, S. H. Mohd-Setapar, C. S. Chuong, A. Khatoon, W. A. Wani, R. Kumar and M. Rafatullah, *RSC Adv.*, 2015, **5**, 30801–30818.
10 H. Du, Z. Wang, Y. H. Chen, Y. Y. Liu, Y. S. Liu, B. J. Li, X. Y. Wang and H. Q. Cao, *RSC Adv.*, 2015, **5**, 10033–10039.
11 Y. Y. Liu, S. M. Wang, C. C. Xin, H. Du, C. X. Du and B. J. Li, *ACS Omega*, 2016, **1**, 491–497.
12 Y. S. Liu, X. Q. Jiang, B. J. Li, X. D. Zhang, T. Z. Liu, X. S. Yan, J. Ding, Q. Cai and J. M. Zhang, *J. Mater. Chem. A*, 2014, **2**, 4264–4269.
13 T. F. Jiao, Y. Z. Liu, Y. T. Wu, Q. R. Zhang, X. H. Yan, F. M. Gao, A. J. P. Bauer, J. Z. Liu, T. Y. Zeng and B. B. Li, *Sci. Rep.*, 2015, **5**, 12415.
14 L. T. Gibson, *Chem. Soc. Rev.*, 2014, **43**, 5173–5182.
15 M. T. Yagub, T. K. Sen, S. Afroze and H. M. Ang, *Adv. Colloid Interface Sci.*, 2014, **209**, 172–184.
16 V. Suba and G. Rathika, *J. Adv. Phys.*, 2016, **5**, 277–294.

 This journal is © The Royal Society of Chemistry 2017

Open Access Article. Published on 16 Januar 2017. Downloaded on 16.02.26 20:25:33.
This article is licensed under a Creative Commons Attribution 3.0 Unported Licence.

17 L. Y. Zhang, W. L. Zhang, Z. Q. Zhou and C. M. Li, *J. Colloid Interface Sci.*, 2016, **476**, 200–205.
18 X. L. Wu, Y. P. Shi, S. X. Zhong, H. J. Lin and J. R. Chen, *Appl. Surf. Sci.*, 2016, **378**, 80–86.
19 Y. Qin, L. Wang, C. W. Zhao, D. Chen, Y. H. Ma and W. T. Yang, *ACS Appl. Mater. Interfaces*, 2016, **8**, 16690–16698.
20 I. Duru, D. Ege and A. R. Kamali, *J. Mater. Sci.*, 2016, **51**, 6097–6116.
21 N. U. Yamaguchi, R. Bergamasco and S. Hamoudi, *Chem. Eng. J.*, 2016, **295**, 391–402.
22 B. Liang, P. Zhang, J. Q. Wang, J. Qu, L. F. Wang, X. X. Wang, C. F. Guan and K. Pan, *Carbon*, 2016, **103**, 94–100.
23 D. R. Dreyer, S. Park, C. W. Bielawski and R. S. Ruoff, *Chem. Soc. Rev.*, 2010, **39**, 228–240.
24 W. Wang, T. F. Jiao, Q. R. Zhang, X. N. Luo, J. Hu, Y. Chen, Q. M. Peng, X. H. Yan and B. B. Li, *RSC Adv.*, 2015, **5**, 56279–56285.
25 S. S. Gao, L. Liu, Y. K. Tang, D. Z. Jia, Z. B. Zhao and Y. Y. Wang, *J. Porous Mater.*, 2016, **23**, 877–884.
26 A. A. Markeb, L. A. Ordosgoitia, A. Alonso, A. Sanchez and X. Font, *RSC Adv.*, 2016, **6**, 6913–6917.
27 N. W. Li, M. B. Zheng, X. F. Chang, G. B. Ji, H. L. Lu, L. P. Xue, L. J. Pan and J. M. Cao, *J. Solid State Chem.*, 2011, **184**, 953–958.
28 M. Y. Dong, Q. Lin, D. Chen, X. N. Fu, M. Wang, Q. Z. Wu, X. H. Chen and S. P. Li, *RSC Adv.*, 2013, **3**, 11628–11633.
29 Z. Ding, W. Wang, Y. J. Zhang, F. Li and J. P. Liu, *J. Alloys Compd.*, 2015, **640**, 362–370.
30 A. A. Farghali, M. Bahgat, W. M. A. E. Rouby and M. H. Khedr, *J. Alloys Compd.*, 2013, **555**, 193–200.
31 N. Dong, F. Z. He, J. L. Xin, Q. Z. Wang, Z. Q. Lei and B. T. Su, *Mater. Res. Bull.*, 2016, **80**, 186–190.
32 G. Y. He, J. J. Ding, J. G. Zhang, Q. L. Hao and H. Q. Chen, *Ind. Eng. Chem. Res.*, 2015, **54**, 2862–2867.
33 J. C. Xu, P. H. Xin, Y. Q. Gao, B. Hong, H. X. Jin, D. F. Jin, X. L. Peng, L. Li, J. Gong, H. L. Ge and X. Q. Wang, *Mater. Chem. Phys.*, 2014, **147**, 915–919.
34 S. W. Yuan and L. Zhao, *RSC Adv.*, 2016, **6**, 49769–49776.
35 J. Ding, B. J. Li, Y. S. Liu, X. S. Yan, S. Zeng, X. D. Zhang, L. F. Hou, Q. Cai and J. M. Zhang, *J. Mater. Chem. A*, 2015, **3**, 832–839.
36 L. Z. Bai, Z. P. Li, Y. Zhang, T. Wang, R. H. Lu, W. F. Zhou, H. X. Gao and S. B. Zhang, *Chem. Eng. J.*, 2015, **279**, 757–766.
37 S. P. Wu, J. C. Huang, C. H. Zhuo, F. Y. Zhang, W. C. Sheng and M. Y. Zhu, *J. Inorg. Organomet. Polym. Mater.*, 2016, **26**, 632–639.
38 S. Bai, X. P. Shen, X. Zhong, Y. Liu, G. X. Zhu, X. Xu and K. M. Chen, *Carbon*, 2012, **50**, 2337–2346.
39 W. S. Hummers and R. E. Offeman, *J. Am. Chem. Soc.*, 1958, **80**, 1339.
40 M. Moriya, M. Ito, W. Sakamoto and T. Yogo, *Cryst. Growth Des.*, 2009, **9**, 1889–1893.
41 Y. Cao, S. R. Cai, S. C. Fan, W. Q. Hu, M. S. Zheng and Q. F. Dong, *Faraday Discuss.*, 2014, **172**, 215–221.
42 S. Stankovich, D. A. Dikin, R. D. Piner, K. A. Kohlhaas, A. Kleinhammes, Y. Jia, Y. Wu, S. T. Nguyen and R. S. Ruoff, *Carbon*, 2007, **45**, 1558.
43 F. Tuinstra and J. L. Koenig, *J. Chem. Phys.*, 1970, **53**, 1126–1130.
44 Q. H. Min, X. X. Zhang, X. Q. Chen, S. Y. Li and J. J. Zhu, *Anal. Chem.*, 2014, **86**, 9122–9130.
45 J. Zhao, H. W. Lai, Z. Y. Lv, Y. F. Jiang, K. Xie, X. Z. Wang, Q. Wu, L. J. Yang, Z. Jin, Y. W. Ma, J. Liu and Z. Hu, *Adv. Mater.*, 2015, **27**, 3541–3545.
46 J. I. Paredes, S. Villar-Rodil, P. Solís-Fernández, A. Martínez-Alonso and J. M. D. Tascón, *Langmuir*, 2009, **25**, 5957–5968.
47 M. Zong, Y. Huang and N. Zhang, *Appl. Surf. Sci.*, 2015, **345**, 272–278.
48 M. Barale, G. Lefevre, F. Carrette, H. Catalette, M. Fedoroff and G. Cote, *J. Colloid Interface Sci.*, 2008, **328**, 34–40.
49 L. Cui, X. Guo, Q. Wei, Y. Wang, L. Gao, L. Yan, T. Yan and B. Du, *J. Colloid Interface Sci.*, 2015, **439**, 112–120.